*metals*

*Article*

# Fe-Containing Al-Based Alloys: Relationship between Microstructural Evolution and Hardness in an Al-Ni-Fe Alloy

**Jonas Faria [1,2], Andrei de Paula [1], Cássio Silva [1], Rafael Kakitani [1], André Barros [1], Amauri Garcia [1], Crystopher Brito [3,*] and Noé Cheung [1]**

[1] Department of Manufacturing and Materials Engineering, University of Campinas—UNICAMP, Campinas 13083-860, SP, Brazil; jonasdiasfaria@ifsp.edu.br (J.F.); a248824@dac.unicamp.br (A.d.P.); c189685@dac.unicamp.br (C.S.); rkakitani@fem.unicamp.br (R.K.); a212042@dac.unicamp.br (A.B.); amaurig@fem.unicamp.br (A.G.); cheung@fem.unicamp.br (N.C.)
[2] Federal Institute of Education, Science and Technology of São Paulo—IFSP, São João da Boa Vista 13872-551, SP, Brazil
[3] Department of Aeronautical Engineering, School of Engineering of São João (FESJ), São Paulo State University—UNESP, São João da Boa Vista 13876-750, SP, Brazil
* Correspondence: crystopher.brito@unesp.br

**Abstract:** Recycled Al alloys not only offer environmental and economic benefits but also present a valuable base for the development of innovative materials, such as Al-Ni-Fe alloys. This work particularly focuses on the microstructural changes and hardness of an Al-5Ni-1Fe alloy (wt.%) solidified with an approximate 20-fold variation in cooling rates. For the various microstructural length scales obtained, only the eutectic regions exhibit a uniform pattern, with the eutectic colonies comprising an $\alpha$-Al phase along with $Al_3Ni$ and $Al_9FeNi$ intermetallic compounds. It is shown that microstructural refinement can lead to a 36% increase in hardness. To represent this mathematically, hardness values are associated with the eutectic colony and intermetallic fiber spacings ($\lambda_{EC}$ and $\lambda_{IF}$ is, respectively) using experimental equations based on the Hall–Petch relationship and multiple linear regression. In addition, comparisons are undertaken with Al-5Ni and Al-1Fe (wt.%) alloy samples produced under the same conditions. The Al-5Ni-1Fe alloy exhibits higher hardness values than both the Al-5Ni and Al-1Fe binary alloys. Furthermore, the hardness of the ternary Al-Ni-Fe alloy is sensitive to microstructural refinement, a characteristic absent in the binary alloys. For $\lambda_{IF}^{-1/2}$ = 1.56 $\mu m^{-1/2}$ (coarser microstructure), the Al-5Ni-1Fe alloy exhibits a hardness of about 13% and 102% higher than that of the Al-5Ni and Al-1Fe alloys, respectively, while for $\lambda_{IF}^{-1/2}$ = 1.81 $\mu m^{-1/2}$ (finer microstructure), it demonstrates a hardness of approximately 39% and 147% higher as compared to that of the Al-5Ni and Al-1Fe alloys, respectively. Thus, this research provides experimental correlations that connect hardness, microstructure, and solidification thermal parameters, contributing to a better understanding for the design of as-cast Fe-contaminated Al-Ni-based alloys.

**Keywords:** recycling; Al alloys; solidification; microstructure; hardness

check for updates

**Citation:** Faria, J.; de Paula, A.; Silva, C.; Kakitani, R.; Barros, A.; Garcia, A.; Brito, C.; Cheung, N. Fe-Containing Al-Based Alloys: Relationship between Microstructural Evolution and Hardness in an Al-Ni-Fe Alloy. *Metals* **2023**, *13*, 1980. https://doi.org/10.3390/met13121980

Academic Editors: Martin Heilmaier and Roberto Montanari

Received: 29 October 2023
Revised: 1 December 2023
Accepted: 4 December 2023
Published: 6 December 2023



## 1. Introduction

Recycling Al alloys is considerably more cost-effective and energy-efficient compared to the production of primary alloys, while also preventing the disposal of valuable metals as waste [1]. Owing to this, numerous technologies dedicated to optimizing the benefits of recycling Al alloys have been documented in the scientific community [2,3]. In this context, the incorporation of Fe during recycling is regarded as a challenge, given its potential to restrict the utilization of the recycled alloy due to adverse effects associated with Fe-rich phases [4]. One typical strategy to address this issue involves chemical modification with certain elements such as Mn, Cr, Sr, and Co [5–9]. However, it should also be considered that the incorporation of Fe into Al alloys may also unlock a broader range of possibilities for developing new materials based on Al alloy scraps.

Regarding Al-Ni alloys originally designed for aerospace applications, they may experience impaired mechanical properties after recycling due to the detrimental effects of Fe incorporation. However, these recycled alloys can serve as base materials. For example, Al-Ni-Fe alloys have a strong potential in powder metallurgy and additive manufacturing applications [10,11]. This implies that Fe-contaminated Al-Ni alloy scraps can be highly useful for producing materials for innovative applications considering a potential structural emphasis. Furthermore, Wang et al. [12] recently observed that the Al-5wt.%Ni semi-solid melts, with a trace addition of Fe (0.3 wt%), exhibit high viscosities. This observation indicates the potential for the future practical exploration of the studied alloy in fabricating structural parts through semi-solid processes. Currently, there is considerable interest in Al-Ni-Fe alloys with solute contents of approximately 1 wt.%. According to Wintergerst et al. [13], an AlFeNi alloy (1Fe, 1Ni, 1Mg [wt%]) is expected to be utilized as nuclear fuel cladding for reactors. Although Fe is generally considered detrimental to Al alloys, exploring the potential of new Fe-containing alloys can offer a novel perspective for the Al industry [14]. Therefore, a comprehensive characterization of the Al-5Ni-1Fe alloy can provide valuable insights for the continued exploration of Al-Ni-Fe alloys, with a particular focus on variations in Ni content. Especially recycled Al-Ni alloys, since the presence of Ni is known to play a key role in the elasticity modulus and mechanical strength of these alloys at high temperatures, primarily due to the formation of specific intermetallic compounds (IMCs), such as $Al_3Ni$ particles [15–17].

Previous studies suggested that grain growth-resistant and thermally stable IMCs can be found in Al-Ni-Fe alloys. For instance, Engin et al. [18] characterized the microstructure of an Al-6.5Ni-1.5Fe alloy (wt.%), representative of the eutectic composition, which was manufactured using a Bridgman-type apparatus. They observed the coexistence of an Al-rich matrix, irregular intermetallic colonies with the presence of $Al_3Ni$ rods, and needle-like $Al_9FeNi$ plate phases. Furthermore, Koutsoukis and Makhlouf [19] reported the occurrence of an Al matrix with long $Al_9FeNi$ fibers in an Al-1.75Fe-1.25Ni (wt.%) cast eutectic alloy. Loginova et al. [10] investigated as-cast and laser-melted samples of distinct Al-Ni-Fe alloys. The microstructural pattern in the as-cast samples, named dendritic cells, consisted of dendrites of the Al-based solid solution and primary crystals of the $Al_9FeNi$ phase. Additionally, a eutectic constituent was formed comprising $Al_3$(Ni, Fe) and $Al_9FeNi$ phases. The microstructure of the laser-melted single tracks primarily consisted of the Al-based solid solution and fine eutectic-origin particles.

It is important to consider that the morphology of microstructural phases in Al-Ni-Fe alloys can be highly sensitive to the cooling conditions during their processing [20,21]. Boettinger et al. [22] analyzed Al-3.7Ni-1.5Fe (wt.%) alloy samples produced through different methods and observed significant variations in their microstructure. Samples in the as-cast state were composed of an $\alpha$-Al matrix with a coarse cellular morphology along with large and small blades of $Al_9(Fe, Ni)_2$ and a fine eutectic mixture consisting of $Al_3Ni$ mixed with $\alpha$-Al. Samples produced using melt-spinning in a Cu wheel exhibited varying morphologies depending on the distance from the wheel surface: $Al_9(Fe, Ni)_2$ particles were found within the interior of $\alpha$-Al grains near the wheel, while a microstructure more similar to the as-cast one was observed further from the surface. In the case of electron beam surface melting and resolidification, the morphology of $\alpha$-Al and $Al_9(Fe, Ni)_2$ ranged from a eutectic colony to a cellular structure with an increase in the electron beam velocity.

Given the promising potential applications of Al-Ni-Fe alloys produced from recycled materials, this work aims to contribute to a better understanding of the microstructural evolution and hardness of an Al-5Ni-1Fe alloy (wt.%) solidified under an unsteady-state heat flow regime. It is worth noting that Bouchard and Kirkaldy [23] categorized directional solidification investigations into two types: one involving solidification in a steady-state heat flow, where the temperature gradient ($G_L$) and growth rate ($G_R$) are independently controlled and maintained constant over time; and the other in an unsteady-state heat flow, where $G_L$ and $G_R$ are interdependent and can vary freely over time. The unsteady-state heat regime represents the class of heat flow of most industrial solidification processes.

Al-5Ni and Al-1Fe alloys (wt.%) samples, prepared under similar conditions, are also characterized as references for comparison purposes. It is worth noting that 1 wt.% Fe is a common Fe content found in recycled Al alloys, and that the Al-5wt.%Ni alloy is among the high-interest hypoeutectic compositions of the Al-Ni alloys system [12,24].

## 2. Materials and Methods

### *2.1. Solidification Experiments*

All alloys referenced in this study will be presented in terms of weight percentage (wt.%). The Al-5Ni-1Fe alloy under investigation was produced using commercially pure metals. Initially, Al was melted in an alumina-coated SiC crucible positioned within a muffle furnace (Brasimet, Jundiaí, Brazil), maintained at a temperature of 900 °C. Subsequently, small chips of Ni and Fe were introduced into the molten Al. The resulting alloy was mechanically homogenized using an alumina-coated stainless-steel rod before being returned to the furnace for approximately one hour. This homogenization procedure was repeated once more, followed by the introduction of Ar gas into the molten alloy to eliminate any potential gas inclusions. The molten alloy was then poured into a preheated, stainless-steel, alumina-coated mold heated to 750 °C using surrounding electrical resistances, as depicted in Figure 1. The application of this directional solidification equipment allowed for the fabrication of an Al-5Ni-1Fe alloy casting that experienced various cooling conditions along its length. Through the implementation of a proper cut procedure on the casting, samples with varying microstructural length scales were obtained. It must be stressed that, rather than introducing a novel fabrication approach for the Al-5Ni-1Fe alloy, the directional solidification technique was utilized to produce samples with various microstructural length scales corresponding to different cooling conditions.

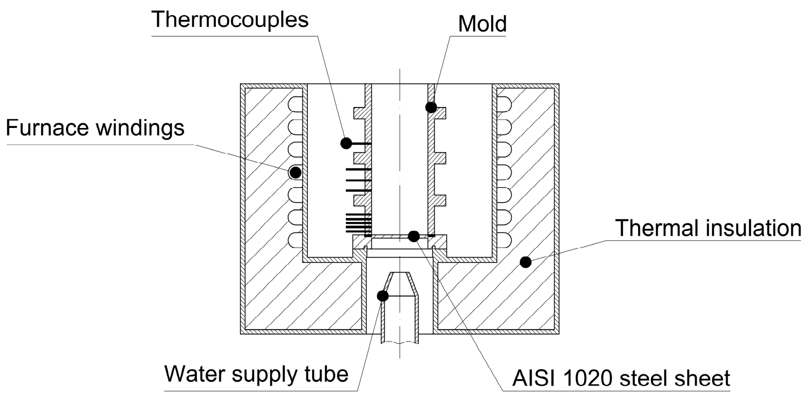


**Figure 1.** Schematic representation of a water-cooled upward directional solidification apparatus.

The cylindrical split mold possessed the internal dimensions of 60 mm in diameter and 150 mm in height and featured passing holes for the placement of thermocouples at nine designated positions (P = 3.5, 7.5, 9, 14, 20, 35, 50, 62, and 85 mm), with the casting base serving as the reference location. Temperature monitoring was conducted at a 5 Hz frequency throughout the cooling process using K-type thermocouples inserted into the molten alloy. These thermocouples were connected to a data logger system (Lynx, São Paulo, Brazil) which, in turn, was linked to a computer for the treatment and recording of thermal data. When the temperature had sufficiently decreased, surpassing the alloy's liquidus temperature ($T_L$) by 5%, the electric heaters were deactivated, and water flow was initiated, marking the initiation of upward directional solidification (DS). It is noteworthy that the mold's base, made of AISI 1020 steel, was not coated with alumina, allowing direct contact with the liquid metal.

### *2.2. Calculation of Solidification Thermal Parameters*

Temperature profiles dependent on time (t) were utilized to assess the evolution of eutectic growth ($V_{eut}$) and cooling rates ($\dot{T}_{eut}$) along the casting length. $V_{eut}$ was determined by calculating the time derivative of a power function $P_{eut} = f(t_{eut})$, where $P_{eut}$ represents the position, and $t_{eut}$ denotes the time when the eutectic isotherm passed from bottom to the top of the directionally solidified (DS) casting. The calculation of $\dot{T}_{eut}$ involved the utilization of power law functions, which were employed to depict the overall behavior of temperature-time data within a comprehensive range surrounding $T_L$. A regression line was employed as long as its coefficient of determination ($R^2$) exceeded 0.9.

### *2.3. Sample Extraction and Metallographic Preparation*

After solidification, the cylindrical DS casting underwent longitudinal sectioning. One of the half-cylindrical halves was subjected to sanding using SiC papers with a range from 100 to 600 mesh, followed by etching with Poulton's solution to reveal the macrostructure. For microstructural examination, samples were extracted from the other cylindrical half of the DS casting. These samples were collected at positions P: 5, 10, 15, 20, 25, 30, 40, 50, 60, 70, and 80 mm from the metal/mold interface, both longitudinally and transversely, corresponding to directions parallel and perpendicular to the vertical growth, respectively. Subsequently, these samples underwent sanding using SiC papers ranging from 100 to 1200 mesh, followed by polishing with diamond paste ranging from 6 to 1 μm. It is worth noting that chemical etching was not necessary to reveal the microstructure. Finally, to assess macrosegregation profiles related to Ni and Fe, X-ray fluorescence (XRF) analyses (model Rigaku RIX, 3100, Tokyo, Japan) were performed on transverse samples.

### *2.4. Microstructural Characterization*

The collection of optical images of the transverse and longitudinal samples was performed using an Olympus GX41 compact inverted metallurgical microscope (Olympus, Tokyo, Japan). In addition, scanning electron microscope (SEM) images were acquired using a Thermo Fisher Scientific Inspect F50 microscope (FEI, Thermo Fisher Scientific, Hillsboro, OR, USA) a ZEISS EVO MA15 SEM (ZEISS-EVO-MA15, Zeiss Microscopy, Oberkochen, Germany), supplemented with an Oxford X-Max model energy-dispersive X-ray spectrometer (EDS) (Zeiss Microscopy, Oberkochen, Germany) for additional characterization.

Despite expecting various microstructural features in the analyzed Al-Ni-Fe alloy, only the eutectic microstructure displayed a consistent pattern that enabled spacing measurements. The intercept method, as described by Gündüz et al. [25], was employed to measure the eutectic colony spacing ($\lambda_{EC}$) and the intermetallic fiber spacing ($\lambda_{IF}$), as shown in Figure 2.

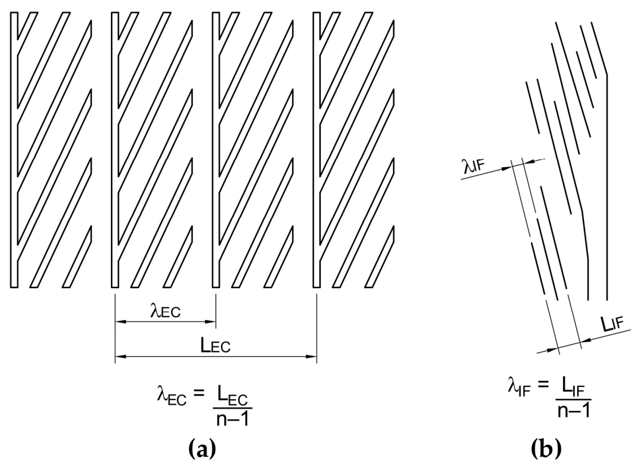


**Figure 2.** Schematic representation of the intercept method employed to measure (**a**) $\lambda_{EC}$ and (**b**) $\lambda_{IF}$.

X-ray diffraction (XRD) spectra were obtained from the transverse samples using a PANalytical X'Pert PRO MRD XL diffractometer (X'Pert Pro MRD XL, Malvern Panalytical, Cambridge, UK). This instrument utilized Cu-Kα radiation with a wavelength of 0.15406 nm, covering the 2θ range from 15° to 90°.

### 2.5. Hardness Testing

The hardness profile of the Al-5Ni-1Fe alloy was assessed following the specifications outlined in ASTM E384-17 standard [26]. For each transverse sample, a minimum of 20 hardness measurements were conducted. These measurements were carried out employing a Future-Tech FV-800 (FV-800, Future-Tech, Kawasaki, Japan) Vickers hardness tester, applying a test load of 1 kgf, and maintaining a dwell time of 15 s.

## 3. Results and Analysis

### 3.1. Solidification Cooling Curves

Figure 3a shows that the DS Al-5Ni-1Fe alloy casting experienced various cooling conditions along its length. It is noteworthy that the temperature drops rapidly near the bottom of the casting but progressively lessens as the distance from the chill increases. Consequently, cooling conditions become less intense toward the top of the casting. Transformation temperatures were verified in the partial pseudo-binary phase diagram of Al-1Fe-Ni alloys, given in Figure 3b, which was calculated by the Thermo-Calc software (TTAL5 database) (Thermo-Calc 2018, Thermo-Calc software, Stockholm, Sweden). At the liquidus temperature, $T_{L,}$ of the studied alloy (673 °C) the formation of the intermetallic compound $Al_9FeNi$ as the primary phase occurs, followed by α-Al at 646 °C. Subsequently, it is expected that the remaining liquid will undergo eutectic transformation at the eutectic temperature ($T_{eut}$) of 640 °C, resulting in the coexistence of the $Al_9FeNi$, α-Al, and $Al_3Ni$ phases. This sequence of transformations aligns with the Scheil–Gulliver (SG) perspective in the solidification path simulated using the Thermo-Calc software with the TTAL5 database, which is shown in Figure 3c. However, it is worth mentioning that the temperatures may exhibit variations due to the non-equilibrium conditions considered in the SG approach.

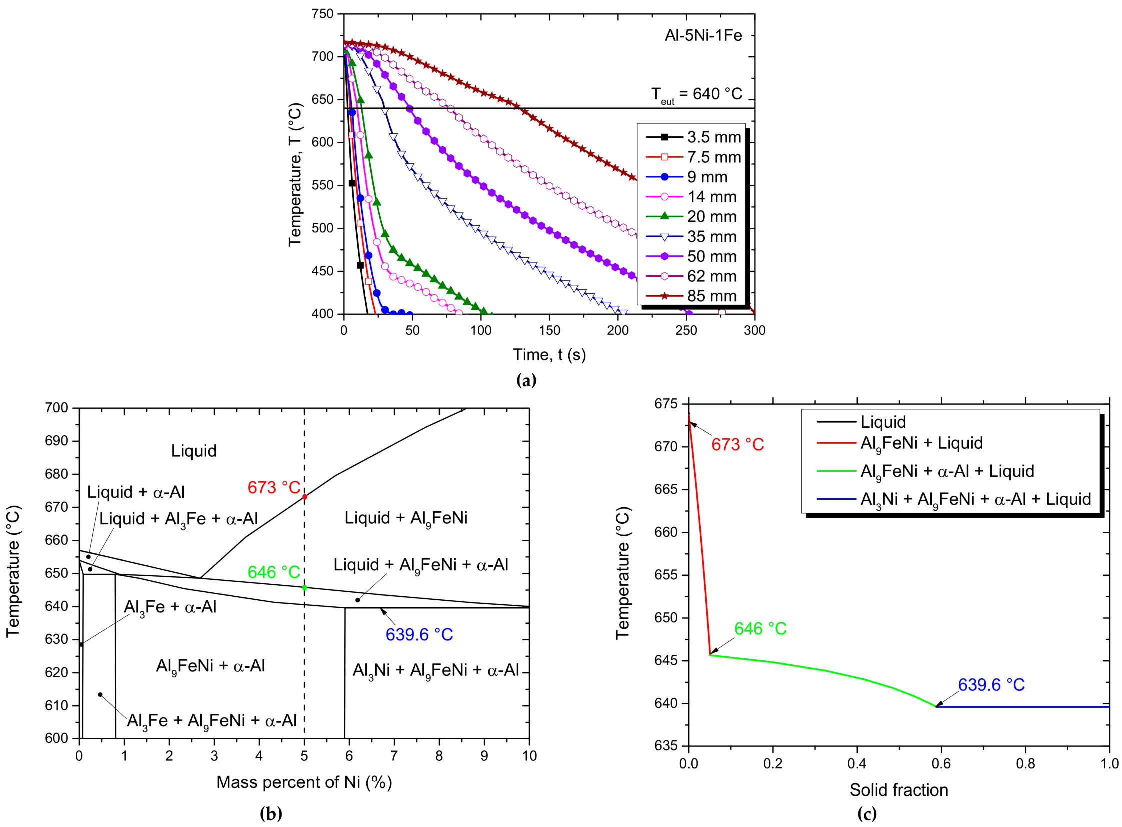


**Figure 3.** (**a**) Cooling curves recorded at different heights from the bottom of the casting for the Al-5Ni-1Fe alloy. (**b**) Partial pseudo-binary phase diagram of Al-1Fe-Ni with a vertical dashed line denoting the Al-5Ni-1Fe alloy composition. (**c**) Scheil–Gulliver solidification path of the Al-5Ni-1Fe alloy.

### *3.2. Macrostructure and Macrosegregation*

The solidification macrostructure of the DS Al-5Ni-1Fe alloy casting is depicted in Figure 4a. As can be seen, it is primarily characterized by columnar grains extending from the bottom to the top of the casting, with no evidence of equiaxed grains. This macrostructure has the typical morphology of directionality castings, i.e., of castings solidified with only one primary heat extraction direction. The macrosegregation profiles for Fe and Ni along the length of the DS Al-5Ni-1Fe alloy casting are presented in Figure 4b. These profiles reveal a brief inverse macrosegregation of Fe and Ni in the region immediately ahead of the cooled bottom surface of the casting. Solute concentrations ranged from approximately ~2.8 wt.%Fe and ~5.6 wt.%Ni at the metal/mold interface to ~1.1 wt.%Fe and ~4.8 wt.%Ni at the top of the DS casting. A similar occurrence of slightly higher Ni concentrations at the base of the DS casting was also observed by Carrara et al. [27] in an Al-8Ni alloy. This phenomenon can be attributed to the elevated cooling rates (30–50 K/s) experienced at the casting's base, along with the limited solubility of Ni in aluminum. Likewise, Fe exhibits low solid solubility in aluminum, of about 10 ppm [28], which may contribute to a comparable segregation behavior as observed for Ni.

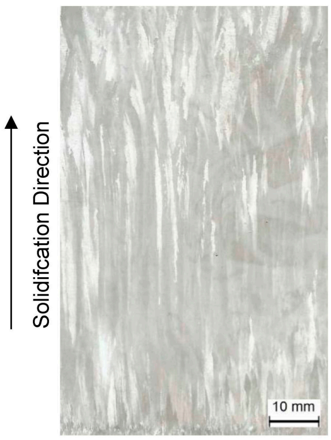


**(a)**

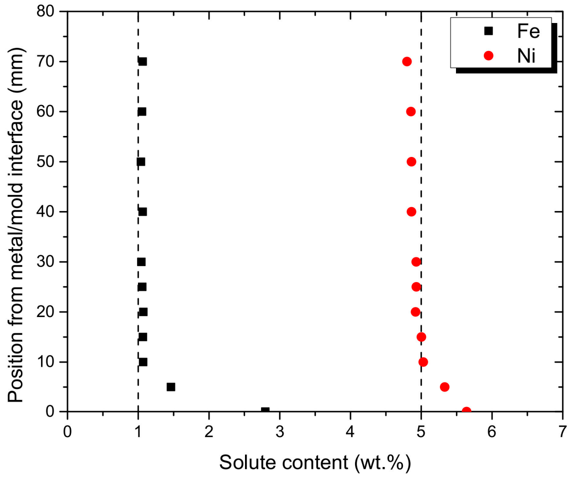


**(b)**

**Figure 4.** (**a**) Solidification macrostructure, and (**b**) profiles of macrosegregation for Fe and Ni along the length of the DS Al-5Ni-1Fe alloy casting.

### *3.3. Solidification Thermal Parameters*

Profiles of $V_{eut}$ and $\dot{T}_{eut}$, represented as functions of the position from the metal/mold interface (P), are depicted in Figure 5a. A gradual decline in both $V_{eut}$ and $\dot{T}_{eut}$ from the metal/mold interface to the top of the DS alloy casting can be identified, which is to be expected. There are two primary contributing factors to this phenomenon: firstly, the rise in thermal resistance with the growth of the solidified shell, and secondly, the formation of voids at the interface between the metal and the mold. Since samples were extracted from the interval between 5 and 70 mm from the metal-mold interface, the ranges of $V_{eut}$ and $\dot{T}_{eut}$ considered for the analysis of the Al-5Ni-1Fe alloy casting span from 0.49 to 1.93 mm/s (approximately a 4-fold change) and 1.16 to 25.06 °C/s (approximately a 20-fold change), respectively. It is worth mentioning that the $V_{eut}$ curve comes from a derivative of the curve that describes the displacement of the eutectic isotherm throughout the experiment. For that reason, there is no coefficient of determination ($R^2$) for the $V_{eut}$ curve. The $R^2$ value shown in Figure 5a is exclusively associated with the $\dot{T}_{eut}$ equation. Figure 5b shows XRD patterns from two samples extracted along the length of the DS casting that represent a faster (P = 10 mm) and a slower (P = 40 mm) cooling regime. The identified phases include α-Al, $Al_3Ni$, and $Al_9FeNi$. Essentially, the unsteady-state solidification conditions promoted by the water-cooled upward directional solidification apparatus are responsible for the formation of the $Al_3Ni$ phase, which is not expected in the partial pseudo-binary phase diagram (Figure 3b) for the Al-5Ni-1Fe alloy. Conversely, in Figure 3c, $Al_3Ni$ is expected to occur, as the determination of the alloy's solidification path takes non-equilibrium conditions into account using the Scheil–Gulliver approach. A possible reason for that is an excess of Ni in the last solid formed, which was sufficient to result in the formation of a non-equilibrium $Al_3Ni$ phase.

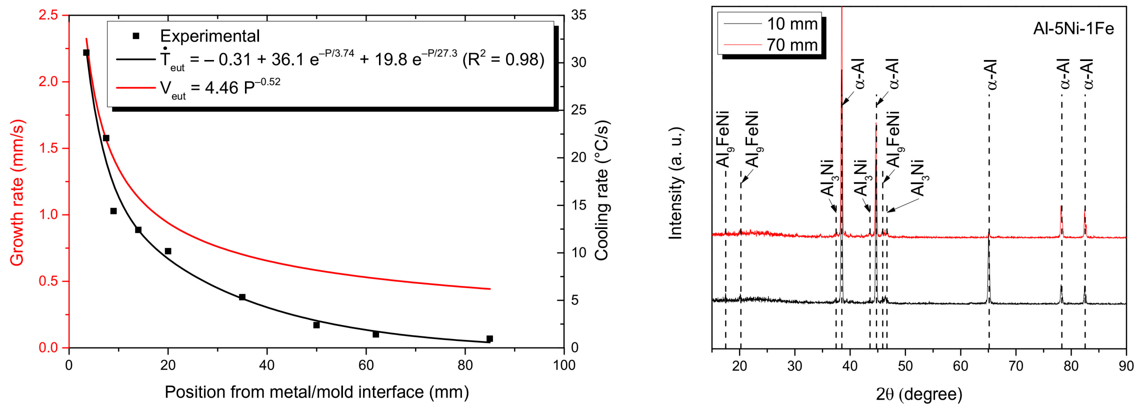


**(a)** **(b)**

**Figure 5.** (**a**) Profiles of $V_{eut}$ and $\dot{T}_{eut}$ as functions of P for Al-5Ni-1Fe alloy casting, and (**b**) XRD patterns obtained from four samples extracted along the length of the DS Al-5Ni-1Fe alloy casting.

### *3.4. Microstructural Analysis*

Figure 6a shows a SEM image with punctual EDS analysis on a longitudinal section of an Al-5Ni-1Fe alloy, cooled at a rate of 1.2 °C/s. The local mass percent concentrations of Al, Fe, and Ni are displayed within the table integrated into this figure. The analysis identified three phases: an α-Al matrix (Spectrum 2), $Al_3Ni$ (Spectrum 4), and $Al_9FeNi$ (Spectrums 1 and 3). Elemental SEM/EDS mapping for an Al-5Ni-1Fe alloy, cooled at a rate of 1.2 °C/s, is depicted in Figure 6b. This mapping illustrates the distribution of elements. The matrix is predominantly composed of Al (red), which is also present in the eutectic colony. The eutectic colony exhibits a significant concentration of Ni (magenta) and trace amounts of Fe (green) as well.

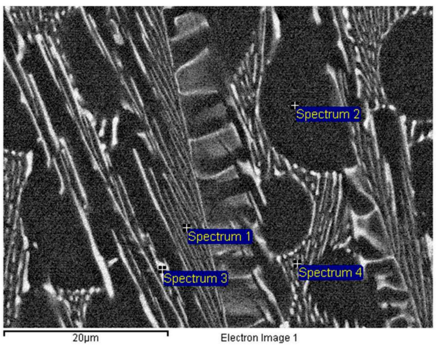


| Spectrum | Mass percent (%) | | |
|---|---|---|---|
| | Al | Fe | Ni |
| 1 | 94.75 | 1.27 | 3.98 |
| 2 | 100.00 | - | - |
| 3 | 82.77 | 0.79 | 16.44 |
| 4 | 94.13 | - | 5.86 |

**(a)**

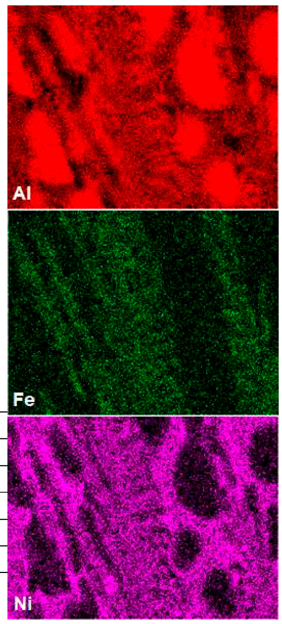


**(b)**

**Figure 6.** (**a**) Solidification macrostructure, and (**b**) profiles of macrosegregation for Fe and Ni along the length of the DS Al-5Ni-1Fe alloy casting.

Figure 7 illustrates the morphology of the intermetallic phases in the Al-5Ni-1Fe, Al-5Ni, and Al-1Fe alloys with greater clarity via SEM images. Each alloy sample underwent an extended chemical etching (aggressive etching) process to enhance the visibility of microstructural features for morphological examination and the analysis of $Al_9FeNi$, $Al_3Ni$, and $Al_6Fe$ intermetallic compounds (IMCs). This step entailed the application of an aqua regia reagent for 3 min for samples of the Al-5Ni-1Fe alloy, selectively removing the Al-rich matrix while preserving other phases in the surrounding areas. For both binary alloys, Al-5Ni and Al-1Fe alloys, the reagent used was a 1 M NaOH solution, and the immersion time was approximately 1 h.

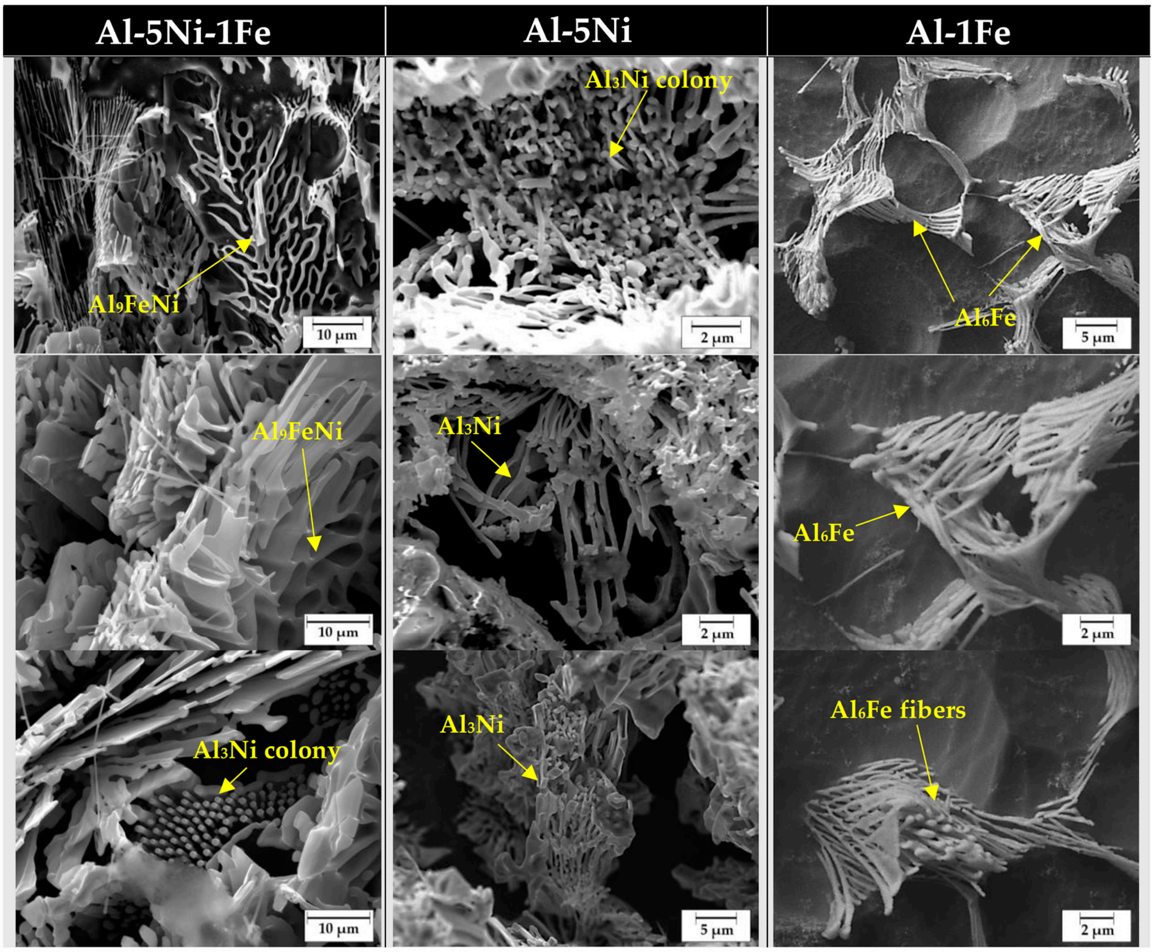


**Figure 7.** SEM images of the Al-5Ni-1Fe, Al-5Ni, and Al-1Fe alloys after an extended chemical etching process (aggressive etching), highlighting the morphology of the intermetallic phases.

Representative longitudinal and transverse images, acquired through optical microscopy, depict the Al-5Ni-1Fe alloy solidified at three distinct cooling rates across the DS casting in Figure 8. The eutectic colony, resembling dendrites, encompasses an $\alpha$-Al matrix along with the intermetallic compounds (IMCs) $Al_3Ni$ and $Al_9FeNi$. Analyzing these micrographs, it becomes evident that there were no significant morphological changes observed along the length of the casting. On the other hand, a more refined microstructural morphology is notably present near the bottom of the DS casting, which can be attributed to the high values of $V_{eut}$ and $\dot{T}_{eut}$ in this specific region. As one moves further away from the metal/mold interface, there is a discernible coarsening of the microstructural morphology. This phenomenon of the growth of larger structures occurs because of the gradual reduction in $V_{eut}$ and $\dot{T}_{eut}$ towards the top of the DS casting.

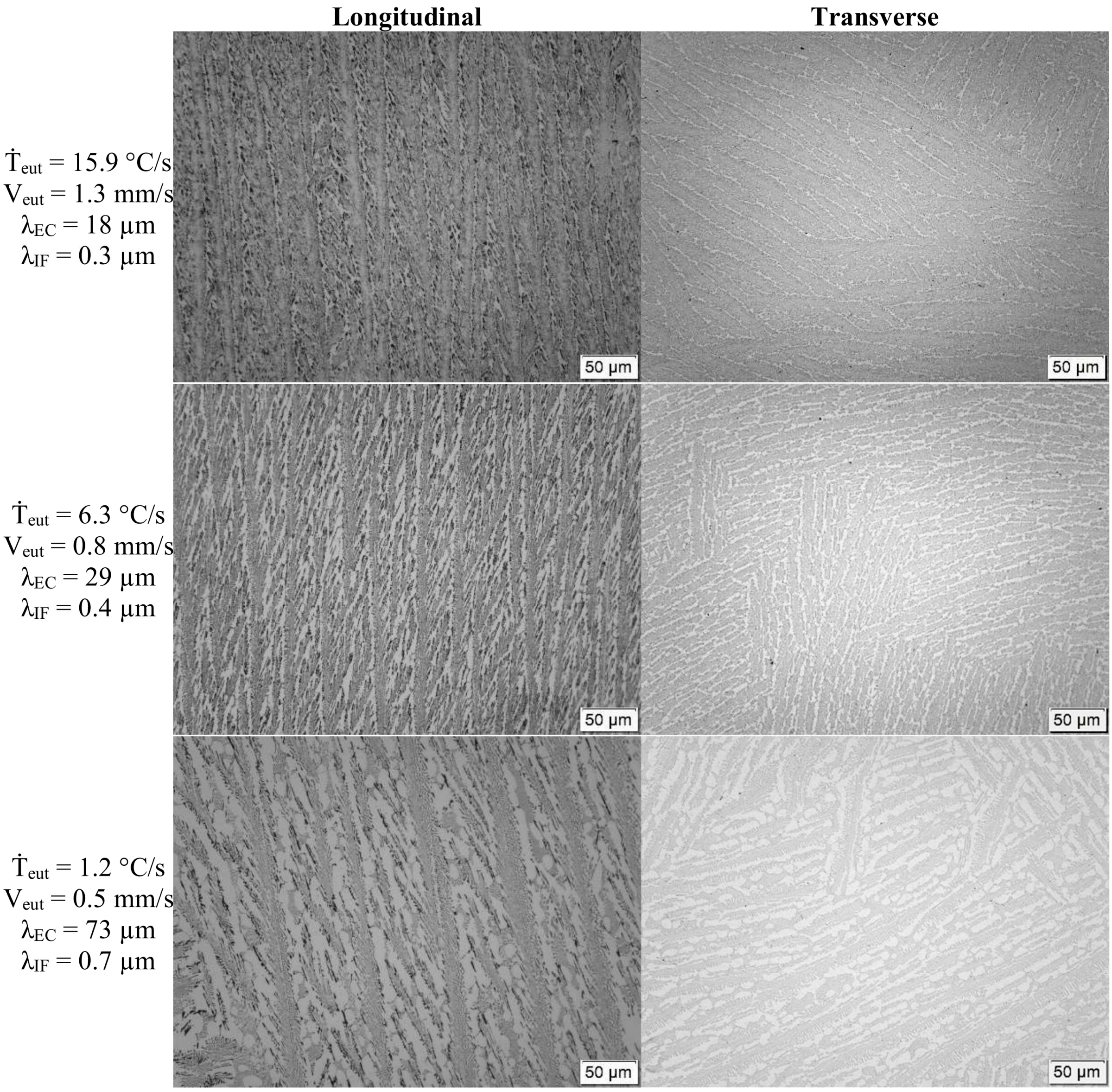


**Figure 8.** Longitudinal and transverse images obtained through optical microscopy of the Al-5Ni-1Fe alloy solidified at 15.9 °C, 6.3 °C/s and 1.2 °C/s cooling rates.

### *3.5. Experimental Correlations among Solidification Thermal Parameters, Microstructural Features, and Hardness*

While various microstructural length scales were recognized along the length of the analyzed Al-Ni-Fe alloy casting, only the eutectic microstructure exhibited a uniform pattern that allowed for the measurement of spacings. Profiles illustrating the variations in eutectic colony and intermetallic fiber spacings with respect to $V_{eut}$ and $\dot{T}_{eut}$ for the Al-5Ni-1Fe alloy casting are shown in Figure 9. The exponents of the experimental power functions for $\lambda_{EC}$ as functions of $V_{eut}$ and $\dot{T}_{eut}$ are −1.1 and −0.55, respectively. These values are consistent with those reported in the literature [29]. Similarly, the exponents of the experimental correlations for $\lambda_{IF}$ in terms of $V_{eu}$t and $\dot{T}_{eut}$ are −0.50 and −0.25, respectively, which align with values reported in the literature [29,30].

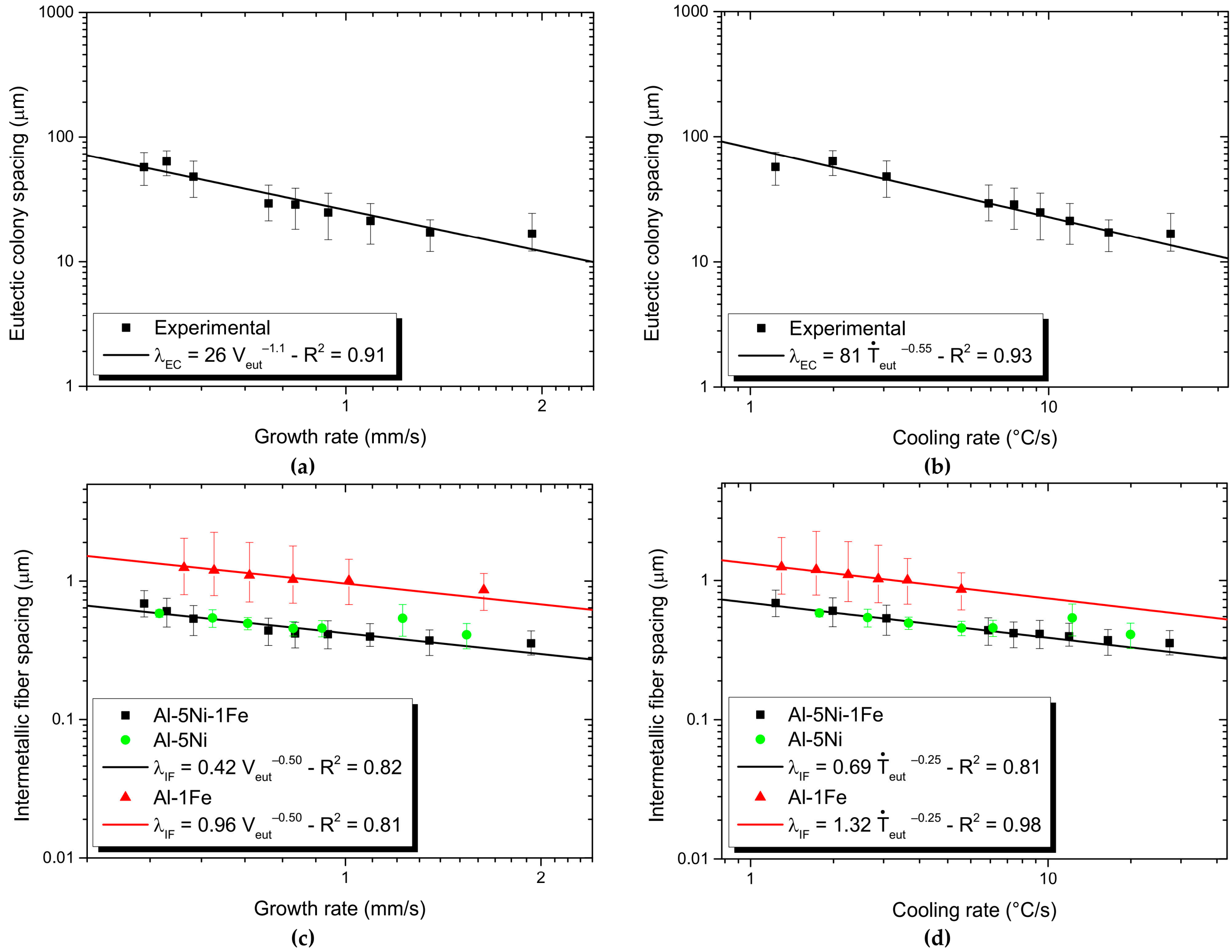


**Figure 9.** Profiles of eutectic colonies spacings as functions of (**a**) growth rate and (**b**) cooling rate for the Al-5Ni-1Fe alloy casting. Profiles of intermetallic fibers spacings as functions of (**c**) growth rate and (**d**) cooling rate for the Al-5Ni-1Fe, Al-5Ni and Al-1Fe alloys.

Figure 10 illustrates the correlation of hardness in the Al-5Ni-1Fe alloy with the inverse of the square root of $\lambda_{EC}$ and $\lambda_{IF}$ (in a Hall–Petch type format), employing a multiple linear regression (MLR) function. A constant value of 48 HV for the Al-5Ni was reported in reference [24] while the Al-1Fe alloy exhibited 27 HV across the entire microstructural range, based on measurements taken from the produced samples. In Table 1, it is noteworthy that the *p*-value is below 5%, describing the significant contribution of the two microstructural parameters ($\lambda_{EC}$ and $\lambda_{IF}$) obtained in the MLR fit. In contrast to the ternary alloy studied here, the other two binary alloys exhibit microstructural phases with more defined morphologies. Hypoeutectic Al-Fe and Al-Ni alloys are known to present cellular [31] and dendritic morphologies [24], respectively. However, the present work does not provide data on cell and dendrite arm spacings, as the only shared microstructural parameter among the three alloys examined is $\lambda_{IF}$. In other words, $\lambda_{IF}$ is measured within the eutectic mixture situated between the cellular and dendritic structures, as well as within the eutectic colonies. It is worth mentioning that measurements of $\lambda_{EC}$ were not available for the mentioned binary hypoeutectic alloys.

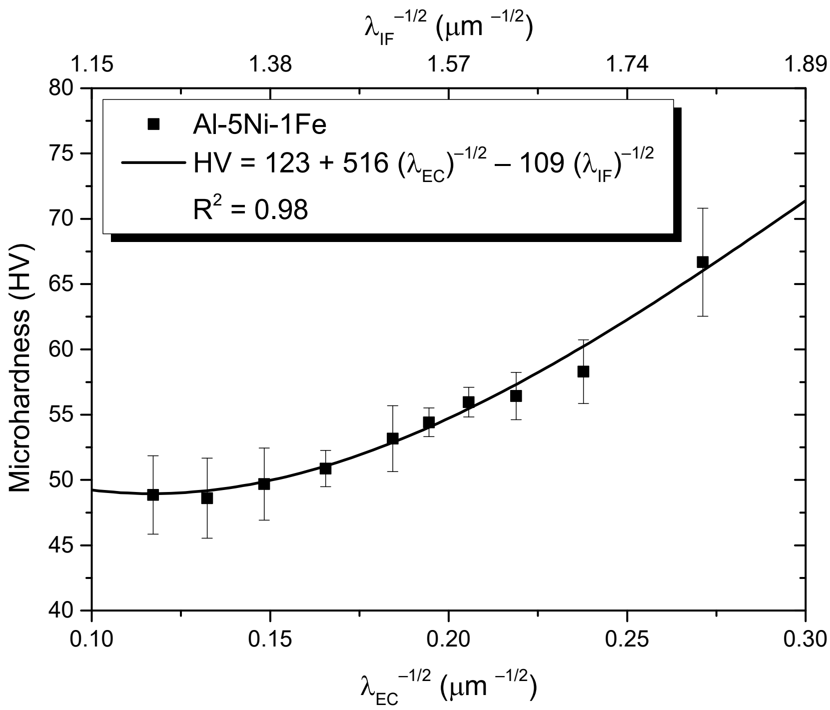


**Figure 10.** Hardness profile of the Al-5Ni-1Fe alloy.

**Table 1.** Results of the MLR analysis for the studied Al-5Ni-1Fe alloy.

| Alloy | Statistical Variable | Statistical Values | | |
|---|---|---|---|---|
| Al-5Ni-1Fe | $R^2$ | 0.98 | | |
| | | Intercept | $(\lambda_{EC})^{-1/2}$ | $(\lambda_{IF})^{-1/2}$ |
| | Coefficient | 122.84 | 515.66 | −109.02 |
| | *p*-value | 0.00035 | 0.00058 | 0.0022 |

In the case of the ternary alloy, a clear increase in hardness is observed as $\lambda_{EC}$ and $\lambda_{IF}$ decrease. In fact, microstructural refinement can result in a remarkable 36% increase in hardness of the Al-5Ni-1Fe alloy, considering the extreme points. Furthermore, the hardness of the Al-5Ni-1Fe alloy exhibits significantly superior values as compared to those of the Al-Fe and Al-Ni binary alloys. The ternary Al-Ni-Fe alloy presents an increase in hardness attributed to its sensitivity to the microstructure refinement, a characteristic not observed in either of the examined binary alloys. Proper comparisons of hardness can be conducted considering common values of $\lambda_{IF}{}^{-1/2}$. For $\lambda_{IF}{}^{-1/2}$ = 1.56 $\mu$m$^{-1/2}$ (indicative of a coarser microstructure) the Al-5Ni-1Fe alloy can surpass the hardness of both the Al-5Ni and Al-1Fe alloys by approximately 13% and 102%, respectively. For $\lambda_{IF}{}^{-1/2}$ = 1.81 $\mu$m$^{-1/2}$ (representing a finer microstructure), the Al-5Ni-1Fe alloy can exceed the hardness of the Al-5Ni and Al-1Fe alloys by approximately 39% and 147%, respectively.

The incorporation of Fe in aluminum-based alloys is frequently viewed as undesirable, especially in Al-Si-based alloys, where it results in the formation of the β-AlFeSi phase [4,32], and Al-Cu alloys, where it leads to the formation of the β-$Al_7Cu_2Fe$ phase [33]. This presence of iron has a detrimental impact on mechanical properties due to the development of these embrittling intermetallic compounds (IMCs) in plate-like structures. Essentially, the Al-5Ni-1Fe alloy can be regarded as an Al-5Ni alloy contaminated with 1Fe. Notably, the hardness profiles of these alloys closely align (Figure 8), suggesting that the IMCs containing both Ni and Fe exhibit a synergistic effect in enhancing mechanical reinforcement. Moreover, the occurrence of the $Al_9FeNi$ IMC in Al-5Cu-0.6Mn-1Fe-(0.5, 1, 1.5)Ni alloys [34], may have played a significant role in improving the mechanical properties of the Fe-contaminated alloys.

## 4. Conclusions

In this study, directionally solidified samples of an Al-5Ni-1Fe alloy underwent comprehensive experimental characterization. The investigation focused on their microstructural evolution and hardness analysis, considering various cooling conditions during the solidification process. Based on the findings, the following conclusions can be drawn:

- Various microstructural length scales revealed a remarkable uniformity in the microstructural pattern where the coexistence of the α-Al, $Al_3Ni$, and $Al_9FeNi$ phases was observed to occur.
- The microstructural refinement achieved in this alloy through variations in the cooling regime during solidification induced a substantial 36% increase in hardness.
- The relationship between hardness (HV) values and the eutectic colony and intermetallic fiber spacings ($\lambda_{EC}$ and $\lambda_{IF}$, respectively) can be represented by a multiple linear regression equation based on a Hall–Petch relationship, as follows $HV = 123 + 516({\lambda_{EC}}^{-1/2}) - 109\ ({\lambda_{IF}}^{-1/2})$, which can be useful for designing as-cast Fe-contaminated Al-Ni-based alloys.
- The hardness of the Al-5Ni-1Fe alloy is approximately 13% and 102% higher than that of the Al-5Ni and Al-1Fe alloys, respectively, for a coarser microstructure. For a finer microstructure, it is about 39% and 147% higher than those of the Al-5Ni and Al-1Fe alloys, respectively.

**Author Contributions:** Conceptualization, J.F., C.B. and N.C.; methodology, J.F., A.d.P., C.S., R.K. and A.B.; validation, J.F., A.d.P., C.S., R.K. and A.B.; formal analysis, J.F., A.d.P., C.S., R.K., A.B., C.B. and N.C.; investigation, J.F.; resources, N.C. and A.G.; data curation, J.F., A.d.P., C.S., R.K., C.B. and N.C.; writing—original draft preparation, J.F., R.K., A.B., A.G. and N.C.; writing—review and editing, C.B., A.G. and N.C.; supervision, C.B., A.G. and N.C.; project administration, A.G. and N.C.; funding acquisition, A.G. and N.C. All authors have read and agreed to the published version of the manuscript.

**Funding:** This research was funded by FAPESP—São Paulo Research Foundation, Brazil (Grants: 2020/09079-2; 2021/11439-0; 2022/15696-0; 2023/01422-8; 2023/12535-8); CNPq-National Council for Scientific and Technological Development–CNPq, Brazil; CAPES—Coordenação de Aperfeiçoamento de Pessoal de Nível Superior, Brazil (Finance Code 001), and FAEPEX/UNICAMP-Fundo de Apoio ao Ensino, à Pesquisa e à Extensão (grants 2162/21 and 2549/22).

**Data Availability Statement:** Data will be made available on request.

**Acknowledgments:** This research used the facilities of the Brazilian Nanotechnology National Laboratory (LNNano), part of the Brazilian Centre for Research in Energy and Materials (CNPEM), a private non-profit organization under the supervision of the Brazilian Ministry for Science, Technology, and Innovations (MCTI). The SEM–FIB staff is acknowledged for their assistance during the experiments (SEM-FIB-C1-20210528) as is the X-ray Diffraction staff (DRXP-20590).

**Conflicts of Interest:** The authors declare no conflict of interest.

## References

1. Raabe, D.; Ponge, D.; Uggowitzer, P.J.; Roscher, M.; Paolantonio, M.; Liu, C.; Antrekowitsch, H.; Kozeschnik, E.; Seidmann, D.; Gault, B.; et al. Making Sustainable Aluminum by Recycling Scrap: The Science of "Dirty" Alloys. *Prog. Mater. Sci.* **2022**, *128*, 100947. [CrossRef]
2. Soo, V.K.; Peeters, J.R.; Compston, P.; Doolan, M.; Duflou, J.R. Economic and Environmental Evaluation of Aluminium Recycling Based on a Belgian Case Study. *Procedia Manuf.* **2019**, *33*, 639–646. [CrossRef]
3. Nunes, H.; Emadinia, O.; Soares, R.; Vieira, M.F.; Reis, A. Adding Value to Secondary Aluminum Casting Alloys: A Review on Trends and Achievements. *Materials* **2023**, *16*, 895. [CrossRef] [PubMed]
4. Basak, C.B.; Meduri, A.; Hari Babu, N. Influence of Ni in High Fe Containing Recyclable Al-Si Cast Alloys. *Mater. Des.* **2019**, *182*, 108017. [CrossRef]

5. Song, D.; Zhao, Y.; Jia, Y.; Li, X.; Fu, Y.; Zhang, W. Synergistic Effects of Mn and B on Iron-Rich Intermetallic Modification of Recycled Al Alloy. *J. Mater. Res. Technol.* **2023**, *24*, 527–541. [CrossRef]
6. Kotadia, H.R.; Qian, M.; Das, A. Microstructural Modification of Recycled Aluminium Alloys by High-Intensity Ultrasonication: Observations from Custom Al–2Si–2Mg–1.2Fe–(0.5,1.0)Mn Alloys. *J. Alloys Compd.* **2020**, *823*, 153833. [CrossRef]
7. Zhang, L.; Gao, J.; Damoah, L.N.W.; Robertson, D.G. Removal of Iron From Aluminum: A Review. *Miner. Process. Extr. Metall. Rev.* **2012**, *33*, 99–157. [CrossRef]
8. Eidhed, M. Modification of β-$Al_5FeSi$ compound in recycled Al-Si-Fe cast alloy by using Sr, Mg and Cr additions. *J. Mater. Sci. Technol.* **2008**, *24*, 45–47.
9. Mahta, M.; Emamy, M.; Daman, A.; Keyvani, A.; Campbell, J. Precipitation of Fe Rich Intermetallics in Cr- and Co-Modified A413 Alloy. *Int. J. Cast Met. Res.* **2005**, *18*, 73–79. [CrossRef]
10. Loginova, I.S.; Sazerat, M.V.; Loginov, P.A.; Pozdniakov, A.V.; Popov, N.A.; Solonin, A.N. Evaluation of Microstructure and Hardness of Novel Al-Fe-Ni Alloys with High Thermal Stability for Laser Additive Manufacturing. *JOM* **2020**, *72*, 3744–3752. [CrossRef]
11. Průša, F.; Vojtěch, D.; Michalcová, A.; Marek, I. Mechanical Properties and Thermal Stability of Al–Fe–Ni Alloys Prepared by Centrifugal Atomisation and Hot Extrusion. *Mater. Sci. Eng. A* **2014**, *603*, 141–149. [CrossRef]
12. Wang, K.; Wei, M.; Liao, Z.; Jin, S.; Wan, B.; Lei, Z.; Tang, P.; Tian, J.; Zhang, L.; Li, W. A comparative Study of Iron, Cobalt or Cerium Micro-Alloying on Microstructure and Apparent Viscosity of Al-5Ni alloy. *J. Alloys Compd.* **2023**, *952*, 170052. [CrossRef]
13. Wintergerst, M.; Dacheux, N.; Datcharry, F.; Herms, E.; Kapusta, B. Corrosion of the AlFeNi Alloy Used for the Fuel Cladding in the Jules Horowitz Research Reactor. *J. Nucl. Mater.* **2009**, *393*, 369–380. [CrossRef]
14. Bian, Z.; Dai, S.; Wu, L.; Chen, Z.; Wang, M.; Chen, D.; Wang, H. Thermal Stability of Al–Fe–Ni Alloy at High Temperatures. *J. Mater. Res. Technol.* **2019**, *8*, 2538–2548. [CrossRef]
15. Czerwinski, F.; Aniolek, M.; Li, J. Strengthening Retention and Structural Stability of the Al-Al3Ni Eutectic at High Temperatures. *Scr. Mater.* **2022**, *214*, 114679. [CrossRef]
16. Kim, T.-S.; Suryanarayana, C.; Chun, B.-S. Effect of Alloying Elements and Degassing Pressure on the Structure and Mechanical Properties of Rapidly Solidified Al–20Si–5Fe–2X (X = Cr, Zr, or Ni) Alloys. *Mater. Sci. Eng. A* **2000**, *278*, 113–120. [CrossRef]
17. Premkumar, M.K.; Lawley, A.; Koczak, M.J. Processing and Microstructure of Powder Metallurgy Al-Fe-Ni Alloys. *Metall. Trans. A* **1992**, *23*, 3219–3230. [CrossRef]
18. Engin, S.; Büyük, U.; Maraşlı, N. The Effects of Microstructure and Growth Rate on Microhardness, Tensile Strength, and Electrical Resistivity for Directionally Solidified Al–Ni–Fe Alloys. *J. Alloys Compd.* **2016**, *660*, 23–31. [CrossRef]
19. Koutsoukis, T.; Makhlouf, M.M. Rendering Wrought Aluminium Alloys Castable by Means of Minimum Composition Adjustments. *Int. J. Cast Met. Res.* **2017**, *30*, 231–243. [CrossRef]
20. Bian, Z.; Liu, Y.; Dai, S.; Chen, Z.; Wang, M.; Chen, D.; Wang, H. Regulating Microstructures and Mechanical Properties of Al–Fe–Ni Alloys. *Prog. Nat. Sci. Mater. Int.* **2020**, *30*, 54–62. [CrossRef]
21. Tiwary, C.S.; Kashyap, S.; Kim, D.H.; Chattopadhyay, K. Al Based Ultra-Fine Eutectic with High Room Temperature Plasticity and Elevated Temperature Strength. *Mater. Sci. Eng. A* **2015**, *639*, 359–369. [CrossRef]
22. Boettinger, W.J.; Bendersky, L.A.; Schaefer, R.J.; Biancaniello, F.S. On the Formation of Dispersoids during Rapid Solidification of an AI-Fe-Ni Alloy. *Metall. Trans. A* **1988**, *19*, 1101–1107. [CrossRef]
23. Bouchard, D.; Kirkaldy, J.S. Prediction of Dendrite Arm Spacings in Unsteady-and Steady-State Heat Flow of Unidirectionally Solidified Binary Alloys. *Metall. Mater. Trans. B* **1997**, *28*, 651–663. [CrossRef]
24. Kakitani, R.; Cruz, C.B.; Lima, T.S.; Brito, C.; Garcia, A.; Cheung, N. Transient Directional Solidification of a Eutectic Al–Si–Ni Alloy: Macrostructure, Microstructure, Dendritic Growth and Hardness. *Materialia* **2019**, *7*, 100358. [CrossRef]
25. Gündüz, M.; Çadırlı, E. Directional Solidification of Aluminium–Copper Alloys. *Mater. Sci. Eng. A* **2002**, *327*, 167–185. [CrossRef]
26. *ASTM E384-17*; ASTM E384-17 Standard Test Method for Microindentation Hardness of Materials. ASTM International: West Conshohocken, PA, USA, 2017; pp. 1–40.
27. Carrara, A.P.; Kakitani, R.; Garcia, A.; Cheung, N. Effect of Cooling Rate on Microstructure and Microhardness of Hypereutectic Al–Ni Alloy. *Arch. Civ. Mech. Eng.* **2021**, *21*, 14. [CrossRef]
28. Basak, C.B.; Hari Babu, N. Improved Recyclability of Cast Al-Alloys by Engineering β-Al9Fe2Si2 Phase. In *Light Metals 2017*; Ratvik, A., Ed.; Springer: Cham, Switzerland; New York, NY, USA, 2017; pp. 1139–1147. [CrossRef]
29. Rodrigues, A.V.; Kakitani, R.; Silva, C.; Giovanetti, L.; Dias, M.; Henein, H.; Garcia, A.; Cheung, N. Influence of Minor Additions of Be on the Eutectic Modification of an Al-33wt.%Cu Alloy Solidified under Transient Conditions. *Metals* **2023**, *13*, 94. [CrossRef]
30. Reyes, R.V.; Kakitani, R.; Costa, T.A.; Spinelli, J.E.; Cheung, N.; Garcia, A. Cooling Thermal Parameters, Microstructural Spacing and Mechanical Properties in a Directionally Solidified Hypereutectic Al–Si Alloy. *Philos. Mag. Lett.* **2016**, *96*, 228–237. [CrossRef]
31. Goulart, P.R.; Lazarine, V.B.; Leal, C.V.; Spinelli, J.E.; Cheung, N.; Garcia, A. Investigation of Intermetallics in Hypoeutectic Al–Fe Alloys by Dissolution of the Al Matrix. *Intermetallics* **2009**, *17*, 753–761. [CrossRef]
32. Dinnis, C.M.; Taylor, J.A.; Dahle, A.K. As-Cast Morphology of Iron-Intermetallics in Al–Si Foundry Alloys. *Scr. Mater.* **2005**, *53*, 955–958. [CrossRef]

33. Liu, K.; Cao, X.; Chen, X.-G. Formation and Phase Selection of Iron-Rich Intermetallics in Al-4.6Cu-0.5Fe Cast Alloys. *Metall. Mater. Trans. A* **2013**, *44*, 682–695. [CrossRef]
34. Lin, B.; Zhang, W.; Zheng, X.; Zhao, Y.; Lou, Z.; Zhang, W. Developing High Performance Mechanical Properties at Elevated Temperature in Squeeze Cast Al-Cu-Mn-Fe-Ni Alloys. *Mater. Charact.* **2019**, *150*, 128–137. [CrossRef]